J Nanostruct 16(4): 5054-5070, Autumn 2026

RESEARCH PAPER

Solar-Light-Driven Photodegradation of Eosin Y Dye Using Green-Synthesized Ag/S/ Modified Fe_3O_4 Nanocomposites with Enhanced Photocatalytic Activity

Hisham T. Hamid *, Sirhan M. M

Department of Chemistry, College of Education for Pure Sciences, University of Anbar, Iraq

ARTICLE INFO

Article History:
Received 27 May 2026
Accepted 11 August 2026
Published 01 October 2026

Keywords:
Eosin Y
Fe_3O_4-nanohybrids
Photo degradation
Solar irradiation

ABSTRACT

The degradation of Eosin Y (EY) dye was investigated using four categories of green-synthesized Fe_3O_4-based nanocatalysts: super paramagnetic iron oxide nanoparticles (Fe_3O_4-SPIONs) and three surface-modified nanohybrids: Ag/Fe_3O_4, S/Fe_3O_4, and Fe_3O_4/Fe_3O_4 nanoparticles. Successful functionalization was achieved and confirmed by FTIR, XRD, TEM and FESEM analysis, which showed cubic inverse spinel magnetite (4.6–7.3 nm) with functionalization (10.7–19.2 nm). The photocatalytic experiments were performed by directly irradiating the solutions (12:00-3:00 PM, 49-52°C) under magnetic stirring at pH 3, 7 and 8. The degradation kinetics were found to follow the pseudo-first-order model of the Langmuir-Hinshelwood model. The removal efficiency of EY was performed after 180 min, and the removal efficiency was found to be 96.23–99.21% for all the systems. The highest apparent rate constant (kapp = 0.02139 min^{-1}, 99.10% removal) was obtained for the Ag/Fe_3O_4 at pH 3. This efficiency was explained as due to localized surface plasmon resonance (LSPR) and charge separation at the Schottky junction. S/Fe_3O_4 achieved the highest removal efficiency (99.21%, kapp = 0.02508 min^{-1}) at pH 8 as a result of the dual radicals (SO_4•$^-$ and •OH) formed by the persulfate in these conditions. This process is environmentally friendly for the treatment of wastewater without pH adjustment since the nanocatalysts can operate in a wide pH range (3–8) powered by solar energy.

How to cite this article
Hamid HT, M. M S . Solar-Light-Driven Photodegradation of Eosin Y Dye Using Green-Synthesized Ag/S/ Modified Fe_3O_4 Nanocomposites with Enhanced Photocatalytic Activity. J Nanostruct, 2026; 16(4):5054-5070. DOI: 10.22052/JNS.2026.04.047

INTRODUCTION

The ongoing release of untreated industrial waste into bodies of water has become a global problem that threatens both the health of people and the balance of ecosystems [1,2]. Some of the most dangerous chemicals in such effluents include synthetic dyes, which the textile, paper, and pharmaceutical industries extensively use [3,4]. EosinY, a derivative of xanthines, and Benzidine, a powerful derivative of aromatic amines, are specifically mentioned as important polluters of the environment due to their high stability, low biodegradability, and potential to accumulate in the food chain [5,6]. Not only do these dyes raise the chemical oxygen demand (COD) of water bodies, but they also inhibit the penetration of sunlight, which is critical in the survival of aquatic organisms through photosynthesis [7,8]. Since they have the potential of being mutagenic and

* *Corresponding Author Email: his24u4003@uoanbar.edu.iq*

carcinogenic toxins, eliminating these recalcitrant molecules in wastewater has become a high-priority activity in the environmental engineering discipline [9,10]. The traditional remediation processes, including the biological treatment, coagulation, and adsorption, usually do not provide enough tools to completely mineralise these dyes or to produce secondary waste [11]. Therefore, the Advanced Oxidation Processes (AOPs), especially heterogeneous photocatalysis, have been identified as an extremely efficient and sustainable substitute, capable of producing powerful radicals to break down the organic pollutants into harmless final products such as CO_2 and H_2O [12,13]. Within photocatalytic materials, magnetite (Fe_3O_4) nanoparticles have become eminent due to their high surface area, low toxicity and their magnetic property that enables rapid recovery under the influence of an external magnetic field [14,15]. Nevertheless, the practical use of pure Fe_3O_4 is often hampered by the tendency of photogenerated charge carriers to recombine rapidly and the limited activity of photogenerated charge carriers in the visible light spectrum [16,17]. To overcome these problems, researchers have extensively studied how non-metal dopants hybridize with noble metals. The addition of silver (Ag) nanoparticles makes it possible to form Schottky barriers and harness the Surface Plasmon Resonance (SPR) effect, used to greatly enhance the separation of electrons and holes and the absorption of visible light [18,19]. In addition, the band structure of the catalyst can be modified with the addition of Sulfur (S) and surface stability, preventing particle aggregation and creating more active sites, which can be obtained by the addition of EDTA as a modifying agent [20,21]. In line with the principles of green chemistry, synthesis of these hybrid nanocomposites has changed towards using plant-based extracts, which are environmentally-friendly reducing and capping agents, thereby avoiding the use of toxic chemicals [22] The use of this plant-mediated technique not only provides a production process that is environmentally friendly but also improves the catalytic performance of the materials that are produced as a result of the synergistic action of natural phytochemicals [23,24]. The study is about the solar-light-driven photodegradation of Eosin Y using a unique green-synthesized Ag/S-modified Fe_3O_4 nanocomposite. These enhancements act as a starting point for the present study. This study aims to take advantage of high sun radiation during sunny days to develop an innovative, economical, and recyclable solution for efficient treatment of industrial dye contamination.

MATERIALS AND METHODS

Collection of Plant

Brassica napus leaves were harvested in the Abu Ghraib region of Baghdad, Iraq, in April and May 2025. The plant material is analysed and categorized at the Desert Studies Centre of Anbar University. After removing impurities, the leaves

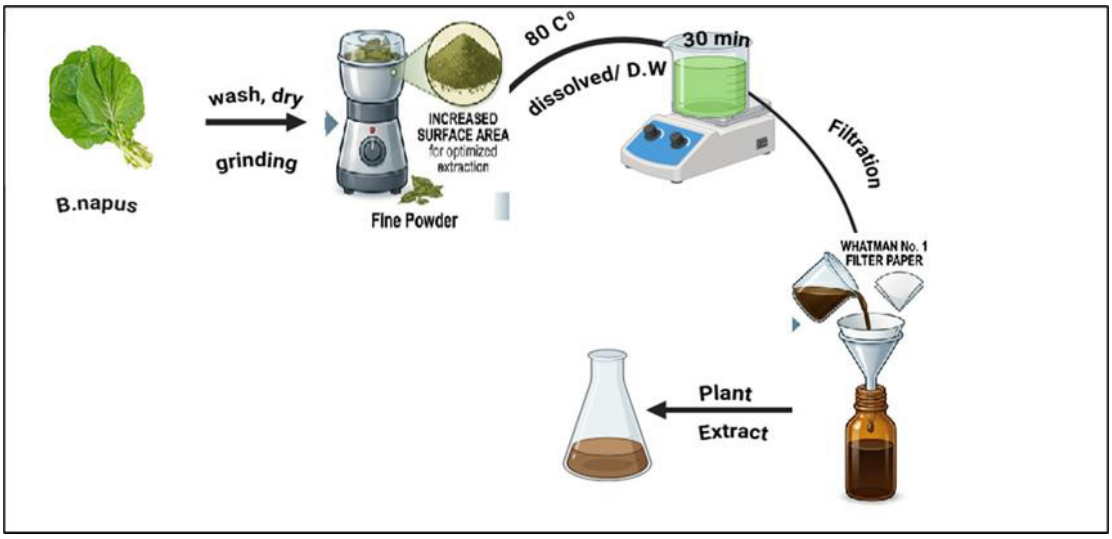

Fig. 1. Schematic of the preparation of *Brassica napus* extract.

were dried in the shade at room temperature, then it was powdered, packed in opaque containers with airtight lids and stored until later study.

Chemicals of Study

Fe $(NO_2)_3 \cdot 6H_2O$ and 25% NaOH were purchased from Fluka and used in the experiment. Throughout the investigation, deionized water (DI) was consistently used. Use of silver nitrate ($AgNO_2$) and Sodium sulphide (Na_2S_2), with 98% analytical purity. Chemicals were obtained from the Sigma-Aldrich company.

Extraction of Crude Extract from Brassica napus

Brassica napus leaves were used to obtain the plant extract. The leaves have been dried, powdered and washed with an electric mixer. All the particulates that were dispersed were removed by sieving. Add 10 g of the powder to a beaker, then add 200 mL of (DI). A magnetic stirrer was used to stir the mixture continuously. Bring to 80°C, stir for 30 mins to obtain the brown extract, and cool. Filtration of the solution ensued. The plant extract was stored in a tumbler bottle in the refrigerator until it was required for use [25].

Green Synthesis of Iron Oxide Nanoparticles (Fe_3O_4)

This experiment was carried out with some slightly modifications. Dissolve 2.2 g of Fe $(NO_3)_2.6H_2O$ in 200 mL of deionized water in a beaker, using a magnetic stir bar. Then carefully add 20 mL of the prepared plant extract. Then, use a burette to add the extract dropwise while stirring vigorously at 20°C. Thereafter, adjust the pH by adding 1 M NaOH and stirring well while increasing the temperature to 80°C. This process will result in a brown precipitate, which is described below. Allow the precipitate to reach room temperature, then centrifuge at 1200 rpm to remove any remaining fibres.

Filter through Whatman No. 1 paper and wash three times with deionized water, followed by a wash with 100% ethanol to remove contaminants; air dry overnight in an oven at 60°C for 2 hr.[25].

Preparation of Ag/S-Fe_3O_4 Nanohybrids

The nanohybrids are synthesized using an impregnation technique with slight modifications to obtain Ag, and S nanoclusters for the nanohybrid production. Add 5 M $AgNO_3$, Na_2S_2, and Fe_3O_4 nanoparticles (green synthesis) in 50 mL DI water. Stir the aggregate in at 80°C darkly. Two hr of synthesis are required at the temperature. The pellet containing particles of Ag, and S-Fe_3O_4 nanohybrids was washed three times with DI water to remove these nanohybrids from the pellet by centrifuging at 1200 rpm for 15 min at 20°C. Ag/S-Fe_3O_4 were purified, oven-dried at 60°C overnight

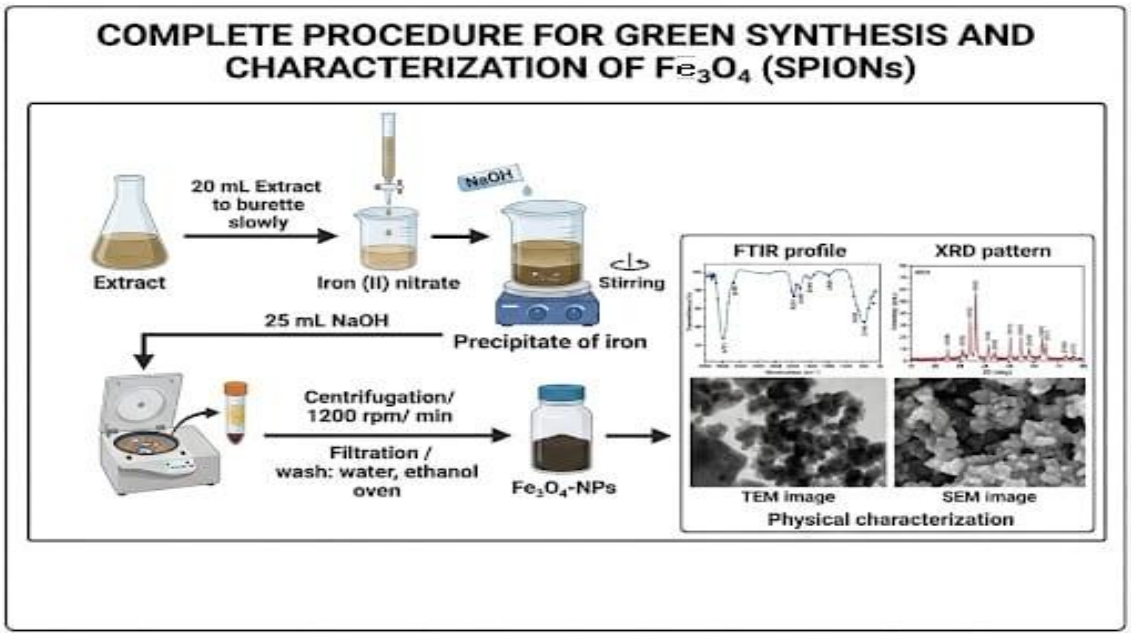

Fig. 2. Diagram of green synthesis and characterization of Fe_3O_4 (SPIONs).

and then powdered in a mortar and pestle [26].

Preparation of Eosin Y and Dye Solution

A certain amount of Eosin Y and dye was separately dissolved in 100 mL of DI to prepare a 1000 ppm stock solution. Then a 20-ppm working solution was made by taking 2 mL of the stock solution and diluting it to 100 mL with DI.

Spectrophotometric Determination and Calibration

For quantitative monitoring of the photodegradation process, a set of standard solutions of Eosin Y dye were prepared, ranging from 5 to 25 ppm. The UV-Vis absorption spectra showed a clear maximum absorption wavelength, λ_{max}, which was 516 nm, as shown in Fig. 4. Thus, the same wavelength was used throughout the remainder of the construction of the standard calibration curve shown in Fig. 5.

Calibration Curve and Quantitative Analysis of Eosin Y dye:

The analytical data showed a strong linear relationship between absorbance and

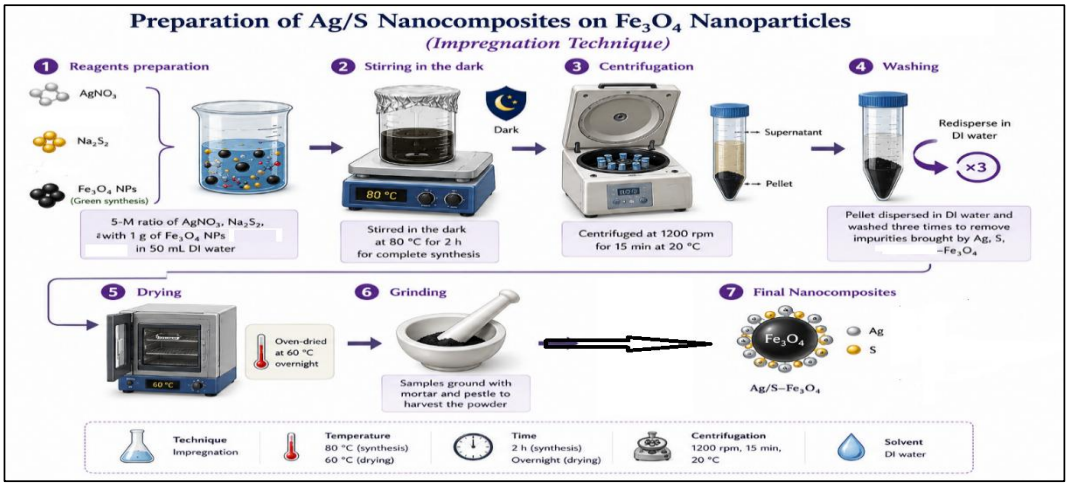

Fig. 3. Schematic representation of Ag/S-Fe_3O_4 nanocomposites preparation by impregnation technique.

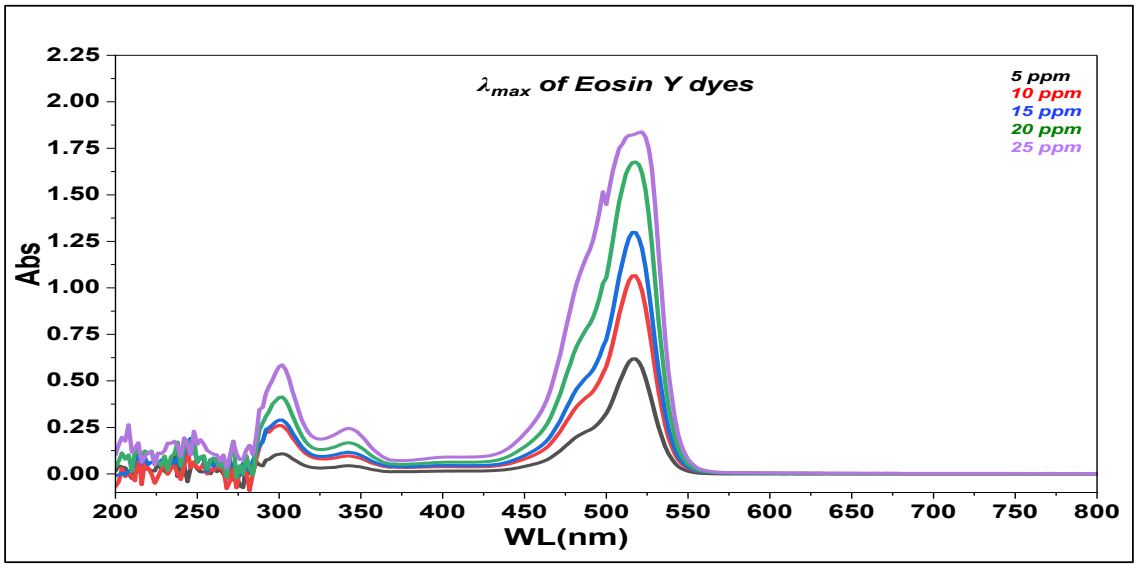

Fig. 4. Shows UV-Vis absorption spectra of Eosin Y dye at various concentrations (5–25 ppm) λ_{max} range.

concentration with a correlation coefficient (R) of 0.9995, which was satisfactory and in good agreement with the Beer-Lambert law. The resulting linear regression equation is:

$$Abs = 0.0597 \cdot C + 0.0010$$

MATERIALS AND METHODS

Photocatalytic Degradation Procedures

The photocatalytic activity of the synthesized nanohybrids (Fe_3O_4, Ag/Fe_3O_4, and S/Fe_3O_4) was evaluated by the degradation of Eosin Y under natural solar light. The effect of medium acidity/alkalinity was investigated at three different levels: pH 3, pH 7 and pH 8, which optimized the catalytic performance.

The reaction Setup and Optimization of pH

In each experimental run, 0.1 g of the photocatalyst was added to 100 mL of the dye solution (20 ppm). The following procedure was carefully followed:

1- pH Adjustment: The pH of the dye solutions was adjusted to the desired values of 3, 7 and 8 with small quantities of the solutions of HCl and NaOH. The pH was adjusted by adding HCl (0.1 N) or NaOH (0.1 N), and it was measured by a pH meter.

2- Dark Adsorption Phase: The suspension was stirred in the dark for 30 min on a magnetic stirrer to attain adsorption-desorption equilibrium. Thus, the subsequent drop in absorbance was solely attributed to photocatalytic degradation and not just physical adsorption.

3- Solar Irradiance: The stabilized suspensions were then subjected to the direct sunlight at the highest level of radiation (12:00 PM – 3:00 PM) at 49 to 52°C. A magnetic stirrer was used continuously during the irradiation time to obtain a uniform suspension of the catalyst particles and to increase the interaction between the catalyst particles and the incident solar photons.

Sampling and Instrumental Analysis

Time Intervals: Aliquots of 5 mL were collected periodically every 30 minutes (0, 30, 60, 90, 120, 150, and 180 min). Centrifugation: The samples were centrifuged immediately after each reaction to separate the solid photocatalysts and end the reaction. Absorbance measurements were used to measure residual concentration, which was obtained with a UV-Vis spectrophotometer. Absorbance values at t=0 (A_o) and at the different times of irradiation (A_t) were measured at the λmax for Eosin dye.

The efficiency and Rate of Reactions/ Calculated

The degradation efficiency (%R) was calculated

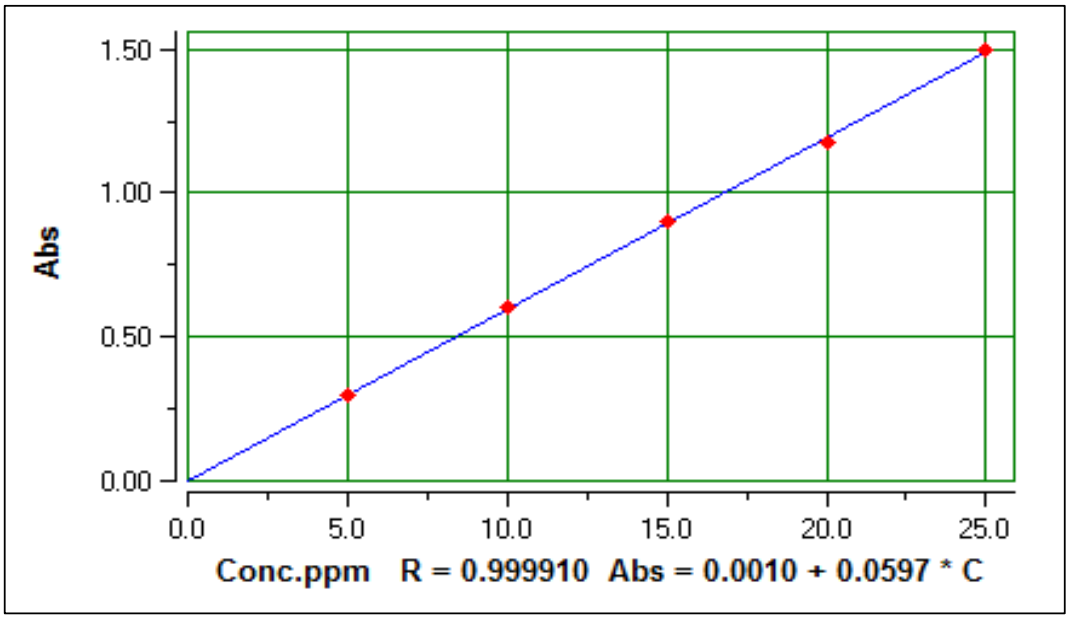

Fig. 5. Standard calibration curve of Eosin Y dye recorded at λ_{max} = 516 nm.

using the following expression:

$$\%R = A_0 - A_t/A_0 \times 100$$

The pseudo-first-order kinetic model was used to appraise the reaction rates.

The rate constant k was computed from the slope of the linear plot of the data $\ln(A_o/A_t)$ vs irradiation time t [27].

$$\ln(A_0/A_t) = k.t$$

Characterization

The main goal of these measurements was to characterize the shape, morphology and structure of the synthesized nanomaterials. The change in colour of the reaction mixture was visually observed, and this change in colour indicates the formation of nanoparticles. FTIR spectroscopy was performed to identify functional groups, which were present in Fe_3O_4-NPs and nanohybrids, in the range 400-4000 cm^{-1} [28]. X-ray diffraction (XRD; Panalytical X'Pert Pro) with Cu-Kα radiation (λ = 1.540 Å, 40 keV, 15 mA) was performed on the as-synthesized samples by performing scans in the 2θ angular range from 10° to 80°. The synthesized Fe_3O_4-NPs were characterized with regard to size and shape by using transmission electron microscopy (TEM) operated at 200 kV. Moreover, the field-emission scanning electron microscopy (FESEM; JEOL-JSM-7600F) was used to investigate the morphology and surface topography of the biosynthesized nanoparticles and nanocomposites [29].

RESULTS AND DISCUSSION

FTIR Spectral Analysis

The (FTIR) spectra of magnetite (Fe_3O_4) nanoparticles and their nanohybrids (Ag/Fe_3O_4 and S/Fe_3O_4). A wide absorption band between 3475 and 3415 cm^{-1} is due to O–H stretching vibrations. This shows that phenolic compounds and flavonoids are present and are acting as reducing and stabilizing agents. This is in line with recent progress in the synthesis of nanoparticles using plants [30]. The peaks at 16351616 cm^{-1} are either because of the stretching of C=O bonds in amides or vibration of C=C bonds in aromatic rings. This implies that the proteins and polyphenols are sticking to the surface of the nanoparticles, forming a stable layer that covers the nanoparticles. When these molecules stick to the surface of the nanoparticle, they seem to form

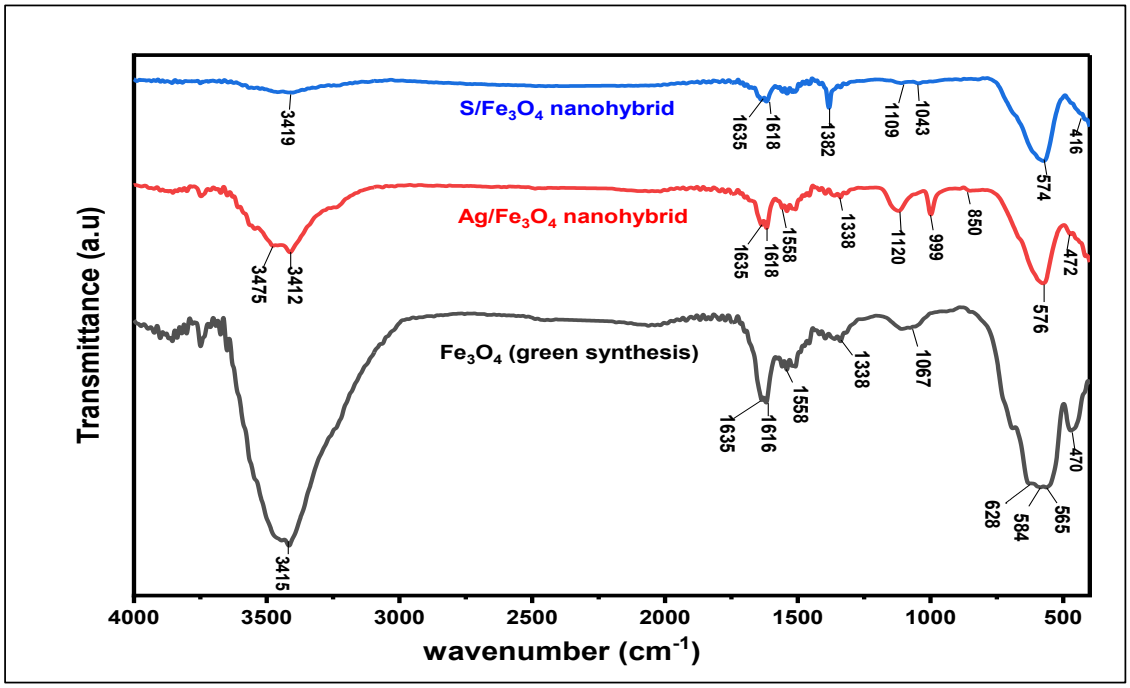

Fig. 6. FTIR spectrum of Fe_3O_4 (SPIONs) synthesized from *Brassica napus* (green synthesis), Ag/Fe_3O_4, and S/Fe_3O_4 nanohybrids.

this layer, which is called a bio-capping layer [31]. The band at a position of 1558 cm^{-1} is designated to the N-H bending (amide II), thus showing that nitrogen-based biomolecules are used to stabilize nanoparticles. The peaks between 1382 and 1338 cm^{-1} are due to C-N stretching or O-H bending, and the peaks between 1109 and 1067 cm^{-1} are because of C-O stretching vibrations. This implies that alcohols and polysaccharides exist and assist in maintaining the stability of the colloids. Extra bands in the 999--850 cm -1 range indicate that the structure has altered due to the addition of silver and its reaction with the Fe_3O_4 matrix. This is in line with recent research on metal–magnetite nanocomposites [32]. The strong absorption bands seen in the low wavenumber range (628–

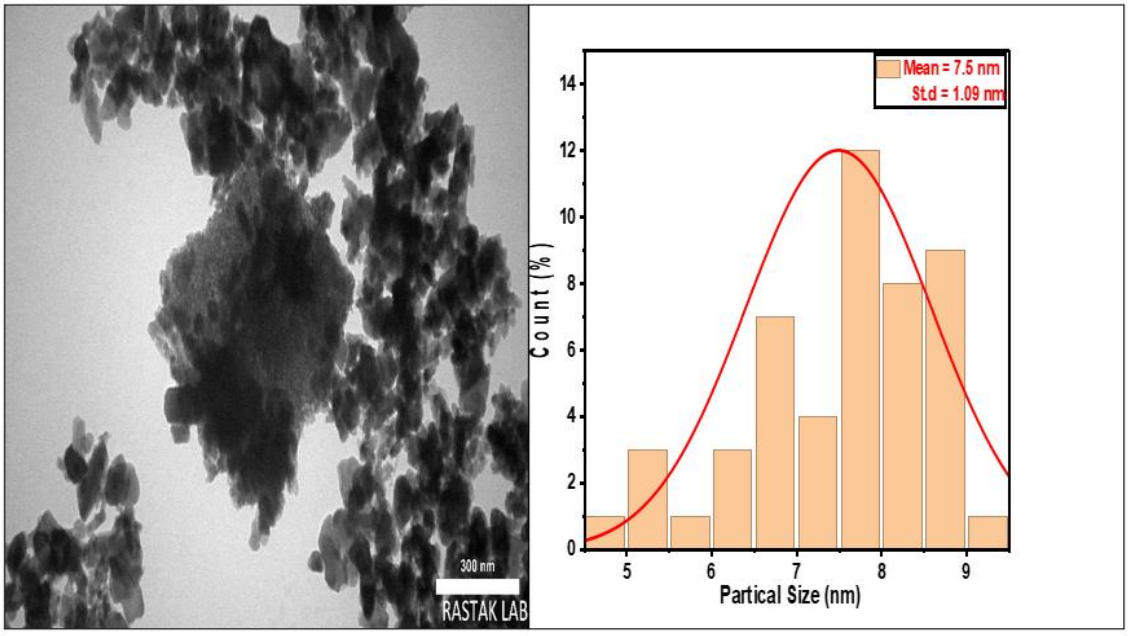

Fig. 7. Represents TEM Fe_3O_4-NPs (green synthesis).

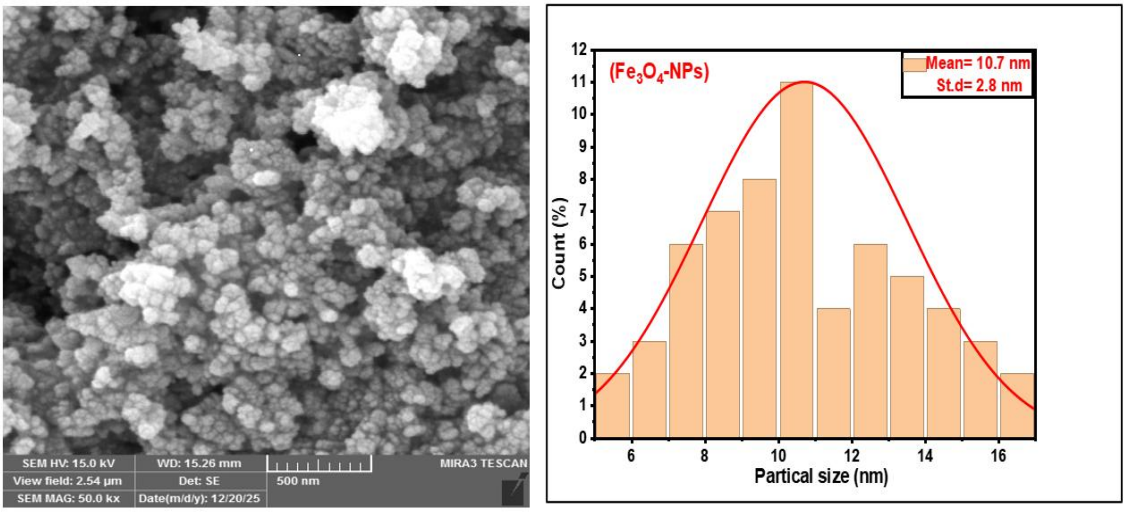

Fig. 8. Represents SEM Fe_3O_4-NPs (green synthesis).

470 cm^{-1}) are typical of Fe–O stretching vibrations, which show that crystalline magnetite has formed. Notably, slight changes in the positions and intensities of the peaks in the nanohybrids compared to pure Fe_3O_4 show that surface functionalization and interfacial interactions have worked, especially in the S/Fe_3O_4 system. This study follows the recent reports, which put a lot of emphasis on the role of surface engineering in enhancing the performance of nanoparticles. These results prove the efficiency of green synthesis using Brassica napus to produce stable and functional nanostructures with promising applications in nanotechnology.

Transmission Electron Microscopy (TEM) Analysis

The quasi-spherical form of synthesized green Fe_3O_4-NPs is densely clustered. Much of this aggregation could be due to the high surface energy of magnetite nanoparticles and the strong magnetic dipole-dipole interactions. This partial aggregation may be due to the fact that the

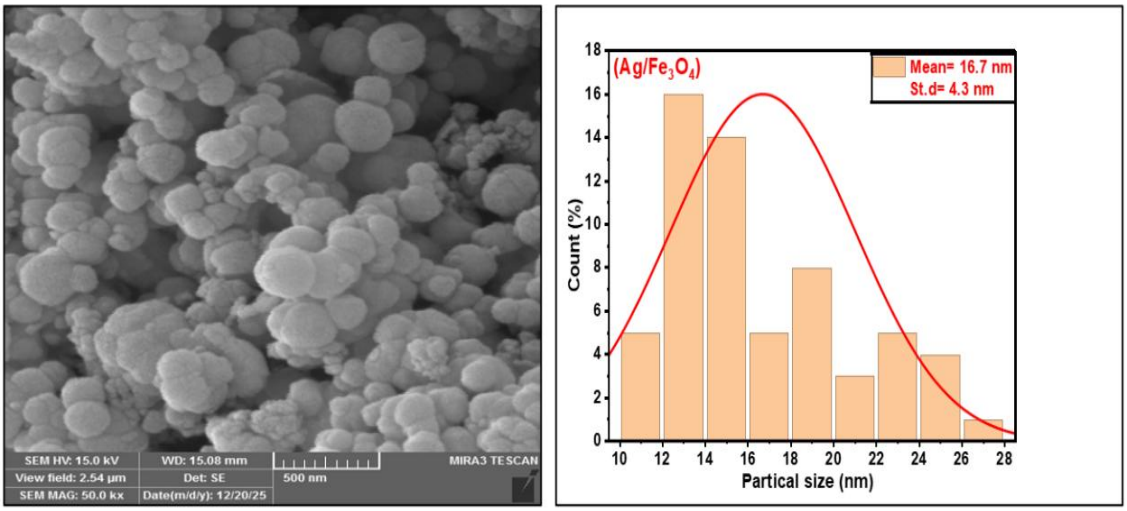

Fig. 9. represents SEM Ag/Fe_3O_4-nanohybrid.

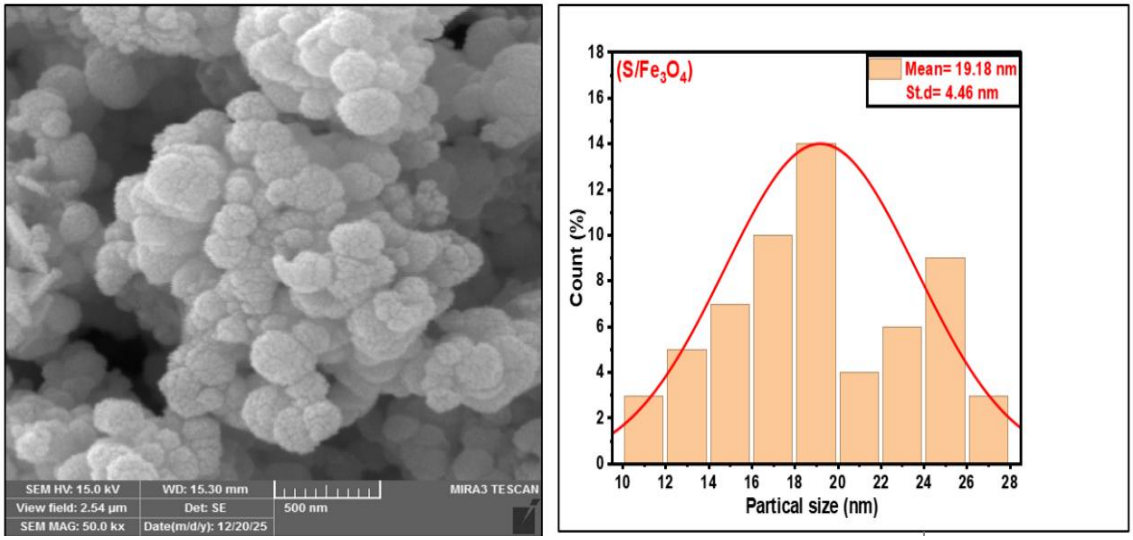

Fig. 10. represents SEM S/Fe_3O_4-nanohybrid.

phytochemicals used for reduction and capping (phenolics, flavonoids, proteins, etc.) are not as effective as synthetic surfactants in stabilizing the micrograph [33]. The result of agglomeration was obtained, but the basic particles were also homogeneous and small, showing that the green synthesis process controlled the nucleation and growth.

Fig. 7 shows the particle size distribution of the synthesized nanogels in the form of a histogram, with a mean particle size of 7.5 nm and an SD of 1.09 nm, indicating a fairly narrow size range. As expected from a well-controlled, reproducible synthesis, the red Gaussian fitted curve shows a regular particle size distribution. Optimized synthesis parameters (pH, temperature and extract concentration) influence reduction kinetics and particle stabilization, leading to excellent uniformity [34]. The small size (<10 nm) of the Fe_3O_4 nanoparticles indicates that these may be superparamagnetic, which is advantageous for medical uses, including targeted drug delivery, hyperthermia therapy and MRI. Just like the green synthesis of magnetite nanoparticles, this method could be employed for the synthesis of functional nanomaterials because of the structural features, small size, quasi-spherical shape, and acceptable dispersion [35]. Overall, TEM and particle size

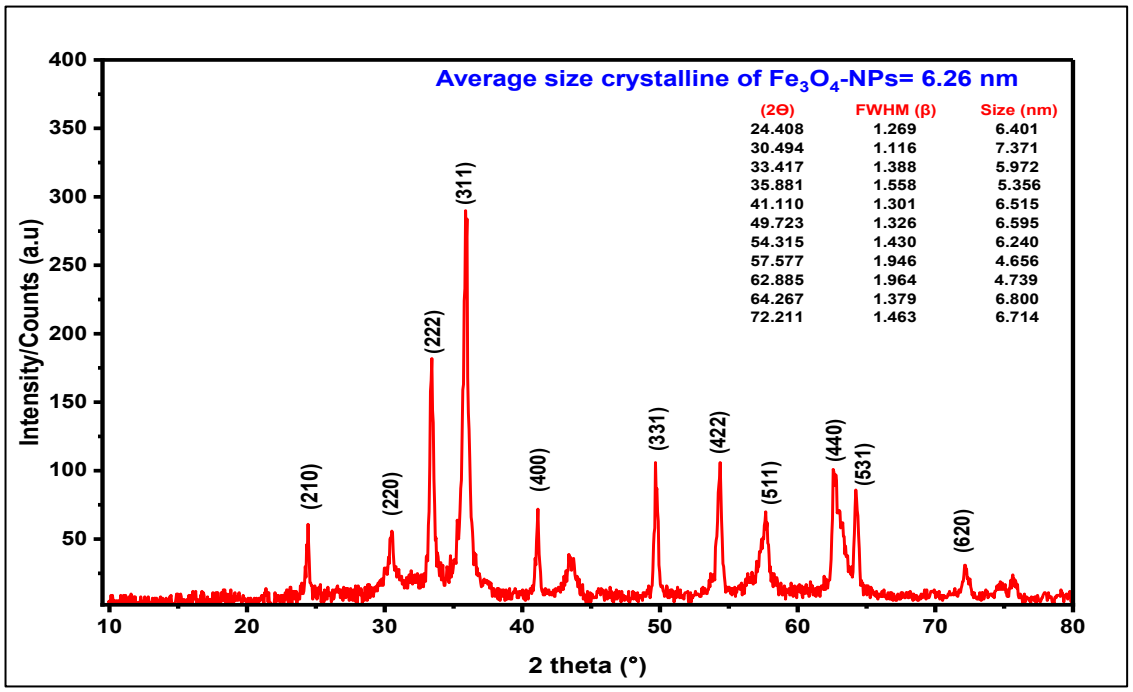

Fig. 11. Shows Fe_3O_4-NPs XRD pattern (green synthesis). The pattern has distinct diffraction peaks for different crystallographic planes. This suggests a spinel cubic structure. 19-0629 JCPDS card.

Table 1. Photodegradation of Eosin Y using green-synthesised Fe_3O_4 (SPIONs) at pH3, 49–52 °C.

Time (min)	A_o	A_t	%R	A_o/A_t	$Ln(A_o/A_t)$
0	1.221	0	0	0	0
30	1.221	0.151	87.63	8.09	2.09
60	1.221	0.092	92.47	13.27	2.58
90	1.221	0.081	93.37	15.07	2.71
120	1.221	0.067	94.51	18.22	2.90
150	1.221	0.058	95.25	21.05	3.05
180	1.221	0.046	96.23	26.54	3.28

studies indicate that the Fe_3O_4 nanoparticles were successfully synthesized using the green synthesis method, yielding homogeneous, ultrasmall nanoparticles with minimal aggregation, which are typical of magnetic nanomaterials.

Field Emission Scanning Electron Microscopy (FESEM) Analysis

The structural changes post-hybridization with Ag, and S are important to understand the particle size (mean=10.7 nm, SD=±2.8 nm) of the Fe_3O_4 nanoparticles green synthesized using the extract of Brassica napus. The small mean size and moderate standard deviation reflect the efficiency of the green synthesis approach in nucleation and regulation of growth. Data of dispersion imply that the reduction mediated by phytochemicals is unpredictable. The bioactive compounds phenolics, flavonoids and proteins present in Brassica napus plant extracts, although having a reducing and capping action, have a less stabilizing effect than synthetic surfactants, resulting in partial aggregation and mild polydispersity [36]. Fig. 8 shows the Fe_3O_4 NP size, and the results for nanohybrids show a systematic increase in particle size for Ag-prepared (16.7 nm (SD ± 4.3 nm)) and S-prepared (19.18 nm (SD ± 4.46 nm)). This increase is due to the fact that secondary components often influence nucleation and crystal development, allowing for effective surface modification and hybrid formation.

Fig. 9 shows that the coated Ag/Fe_3O_4 nanoparticles form a core/shell structure on Fe_3O_4. The Ag^+ ions used in the synthesis could have increased the number of nucleation centres and the heterogeneous growth, and thus the expansion of the particles and larger size dispersion [33]. Silver atoms may also reduce surface energy differences, improving partial particle coalescence [37]. Furthermore, atoms of silver could decrease the differences in surface energy and promote partial coalescence of

Table 2. Photodegradation of Eosin Y using Ag/Fe_3O_4 nanohybrid at pH3, 49–52 °C.

Time (min)	A_o	A_t	%R	A_o/A_t	$Ln(A_o/A_t)$
0	1.541	0	0	0	0
30	1.541	0.202	86.89	7.63	2.03
60	1.541	0.163	89.42	9.45	2.25
90	1.541	0.088	94.29	17.51	2.86
120	1.541	0.054	96.50	28.54	3.35
150	1.541	0.043	97.21	35.84	3.58
180	1.541	0.028	98.19	98.18	4.59

Table 3. Photodegradation of Eosin Y using S/Fe_3O_4 nanohybrid at pH 3, 49–52°C.

Time (min)	A_o	A_t	%R	A_o/A_t	$Ln(A_o/A_t)$
0	1.193	0	0	0	0
30	1.193	0.063	94.72	18.94	2.94
60	1.193	0.056	95.31	21.30	3.06
90	1.193	0.041	96.56	29.10	3.37
120	1.193	0.032	97.32	37.28	3.62
150	1.193	0.023	98.07	51.87	3.95
180	1.193	0.014	98.83	85.21	4.45

Table 4. Comparative summary: removal efficiencies and pseudo-first-order rate constants k_{app} (min^{-1}) with R^2 values of all catalytic systems.

Catalyst	A_o	%R (30 min)	%R (180 min)	k_{app} (min^{-1})	R^2	$Ln(A_o/A_t)$ at 180 min
Fe_3O_4 (Green)	1.221	87.63%	96.23%	0.01438	0.7018	3.28
Ag/Fe_3O_4	1.541	86.89%	98.19%	0.02139	0.9061	4.59
S/Fe_3O_4	1.193	94.72%	98.83%	0.01896	0.7244	4.45

adjacent particles [37]. The S/Fe_3O_4 nanohybrid in Fig. 10 indicated a slight increase in the average size of 19.18 nm and SD of 0.97 nm, which clearly indicated that the incorporation of sulphur had a relatively larger effect on the particle assembly. In SEM micrographs, the process increases particle size, forms particle clusters, and bridges particles through strong bonding and adsorption between Fe and S [38]. This is due to the surface chemistry, the deposition of the secondary phase, the organic functionalization, and the interaction between the particles. These factors resulted in small nanoparticles with moderate aggregation (10.7 nm), larger particles surface-decorated with Ag (16.7 nm), and larger and more clustered particles with S (19.18 nm) [39]. All nanoscale systems (< 20 nm) possess superparamagnetic properties, a very high surface area ideal for catalysis, antibacterial activity, and biological uses. The literature suggests that green-made iron oxide nanohybrids develop and change their aggregation state in response to changes in surface energetics or reaction pathways [40].

X-ray diffraction (XRD) analysis

The XRD pattern of green synthesized Fe_3O_4 nanoparticles exhibits sharp peaks at 2θ 30, 35, 43, 57 and 62 degrees corresponding to crystallographic planes (220), (311), (400), (511) and (440) respectively. The product is found to be consistent with the JCPDS (No. 19-0629) data of cubic inverse spinel magnetite (Fe_3O_4) which indicates the successful synthesis of the product. Literature reports [31,41,42]. The importance of synthesis of Fe_3O_4 nanoparticles using the green technique with respect to the peak position and

Table 5. Photodegradation of Eosin Y using green-synthesised Fe_3O_4 (SPIONs) at pH 7. Solar irradiation: 12:00–3:00 pm, 49–52 °C, continuous magnetic stirring.

Time (min)	A_o	A_t	%R	A_o/A_t	$Ln(A_o/A_t)$
0	1.637	0	0	0	0
30	1.637	0.223	86.38	7.34	1.99
60	1.637	0.148	90.96	11.06	2.40
90	1.637	0.053	96.76	30.89	3.43
120	1.637	0.040	97.55	40.93	3.71
150	1.637	0.035	97.86	46.77	3.85
180	1.637	0.025	98.47	65.48	4.19

Table 6. Photodegradation of Eosin Y using Ag/Fe_3O_4 nanohybrid at pH 7. Solar irradiation: 12:00–3:00 pm, 49–52°C, continuous magnetic stirring.

Time (min)	A_o	A_t	%R	A_o/A_t	$Ln(A_o/A_t)$
0	1.673	0	0	0	0
30	1.673	0.094	94.38	17.80	2.88
60	1.673	0.072	95.70	23.24	3.15
90	1.673	0.054	96.77	30.98	3.43
120	1.673	0.041	97.55	40.80	3.71
150	1.673	0.036	97.85	46.47	3.84
180	1.673	0.015	99.10	111.53	4.71

Table 7. Photodegradation of Eosin Y using S/Fe_3O_4 nanohybrid at pH 7. Solar irradiation: 12:00–3:00 pm, 49–52°C, continuous magnetic stirring.

Time (min)	A_o	A_t	%R	A_o/A_t	$Ln(A_o/A_t)$
0	1.632	0	0	0	0
30	1.632	0.234	85.66	6.97	1.94
60	1.632	0.115	92.95	14.19	2.65
90	1.632	0.068	95.83	24.00	3.18
120	1.632	0.051	96.88	32.00	3.47
150	1.632	0.039	97.61	41.85	3.73
180	1.632	0.023	98.86	70.96	4.26

indexing. High diffraction peak at (311) plane indicates a good orientation and crystalline order of the nanoparticles.

The absence of secondary peaks of haematite (Fe_3O_4) or maghemite (γ-Fe_3O_4) confirms the phase-purity of magnetite and their stabilizing effect in green synthesis [43]. Also, the "broadening" of the diffraction peaks indicates nanoscale particles. Crystallite size was calculated using Debye Scherrer equation.

$$D = 0.9\,\lambda/\beta\cos\theta$$

Average crystallite size ranges from 4.6 to 7.3 nm, with an average crystallite size of 6.26 nm. This value is lower than that of the green synthesized Fe_3O_4 nanoparticles, which are dependent on the synthesis conditions [44]. A comparison of this kind of XRD data to TEM and SEM results revealed a definite and scientifically sound trend. The XRD crystal size is ~6 nm, which is smaller than TEM (~10.7 nm) and SEM (~16-19 nm) measurements. This difference might be due to natural differences in methodology. TEM measures particle size (there may be many crystallite sizes), while XRD measures coherent crystalline domain size. SEM may observe larger agglomerated structures resulting from particle clustering. Capping chemicals present in plant extracts during the preparation of green nanoparticles can cause the particle sizes of TEM and SEM to differ [45].

Photocatalytic Activity

Effect of Green-Synthesized Fe_3O_4 (SPIONs) on Eosin Y Degradation pH3

The UV–Vis absorbance data of Fe_3O_4 nanoparticles, which were synthesized using greenery, are summarized in Table 1 at pH 3 (A_o = 1.221). The surface of Fe_3O_4 is positively charged at pH 3 (below its pH_{pzc} ≈ 6.8), thus increasing the interaction between the dye and the catalyst

Table 8. Comparative kinetic and performance parameters for EY photodegradation at pH 7. The k_{app} values have been determined by linear regression of the log of (A_o/A_t) against irradiation time. See Fig. S2 (a, b, c)

Catalyst	A_o	%R (30 min)	%R (180 min)	k_{app} (min^{-1})	R^2	$Ln(A_o/A_t)$ at 180 min
Fe_3O_4 (Green)	1.637	86.38%	98.47%	0.02095	0.8566	4.19
Ag/Fe_3O_4	1.673	94.38%	99.10%	0.01977	0.7419	4.71
S/Fe_3O_4	1.632	85.66%	98.86%	0.02045	0.8660	4.26

Table 9. Photodegradation of Eosin Y using green-synthesised Fe_3O_4 (SPIONs) at pH 8. Solar irradiation: 12:00–3:00 pm, 49–52 °C, continuous magnetic stirring.

Time (min)	A_o	A_t	%R	A_o/A_t	$Ln(A_o/A_t)$
0	1.595	0	0	0	0
30	1.595	0.282	82.32	5.66	1.73
60	1.595	0.102	93.61	15.64	2.75
90	1.595	0.040	97.49	39.88	3.69
120	1.595	0.032	98.00	49.84	3.91
150	1.595	0.022	98.62	72.50	4.28
180	1.595	0.013	99.18	122.69	4.81

Table 10. Photodegradation of Eosin Y using Ag/Fe_3O_4 nanohybrid at pH 8. Solar irradiation: 12:00–3:00 pm, 49–52°C, and continuous magnetic stirring.

Time (min)	A_o	A_t	%R	A_o/A_t	$Ln(A_o/A_t)$
0	1.051	0	0	0	0
30	1.051	0.120	88.58	8.76	2.17
60	1.051	0.088	91.63	11.94	2.48
90	1.051	0.067	93.63	15.69	2.75
120	1.051	0.042	96.00	25.02	3.21
150	1.051	0.037	96.48	28.41	3.35
180	1.051	0.022	97.91	47.77	3.87

due to the electrostatic attraction between the EY molecule (anionic at pH 3, pKa = 3.8) and the surface. The Fe^{2+}/Fe^{3+} cycling under solar photons further promotes the production of hydroxyl radicals (•OH) for mineralization [46]. The $\ln(A_o/A_t)$ plot (Fig. S1a) presents an almost linear plot, with k_{app} = 0.01438 min^{-1} and an R^2 = 0.7018 value.

Effect of Ag/Fe_3O_4 Nanohybrid on Eosin Y Degradation pH3

The Ag/Fe_3O_4 nanohybrid (A_o = 1.541, Table 2) achieved 98.19% removal at 180 min, with k_{app} = 0.02139 min^{-1} (R^2 = 0.9061), the highest goodness-of-fit among all pH 3 systems. The superiority of kinetic linearity is explained by the synergistic effect of the localized surface plasmon resonance (LSPR) of the Ag nanoparticles, which capture photons from the visible range of the solar spectrum (≈400-450 nm) and put hot electrons into the conduction band of Fe_3O_4. At the Ag–Fe_3O_4 interface, the Schottky junction is formed to inhibit the recombination of electron–hole pairs, which increases the lifetime of the photogenerated holes (h^+) and superoxide radicals ($•O_2^-$) [47]. The Ag–Fe_3O_4 interface, a metal–semiconductor junction, prevents charge recombination and promotes efficient charge transfer. The initial removal at 30 min (86.89%) is slightly lower than Table 1 (87.63%), possibly due to increased initial absorbance (A_o = 1.541 vs 1.221), indicating dye loading is momentarily clogging active sites [48].

Effect of S/Fe_3O_4 Nanohybrid on Eosin Y Degradation pH3

S/Fe_3O_4 (A_o = 1.193, Table 3) exhibited the highest initial removal rate at pH 3, reaching 94.72% within 30 min and 98.83% at 180 min (k_{app} = 0.01896 min^{-1}). By doping Fe_3O_4 with sulphur, mid-gap energy states will be added, which will reduce the optical band gap of Fe_3O_4 and therefore increase the absorption of visible-light photons. Furthermore, the active species produced at the sulphur-functionalised surface, in addition to •OH, [49], gives rise to a dual-radical degradation pathway, making for the quick initial reaction rates. The A_o/A_t and A_o/A_t (Ln) values are high and constant, even at the first time point (2.94 at 30 min), indicating that the catalytic activity of S/Fe_3O_4 is approaching its highest value after the initial exposure to the sunlight.

Pseudo-First-Order Kinetic Analysis pH 3

The pseudo-first-order kinetic plots [$\ln(A_o/A_t)$ vs. irradiation time] Table 5 presents the apparent rate constants k_{app} and the corresponding R^2 values from the linear regression graphs. See Fig. S1a, b, c.

Photocatalysis at Neutral pH 7

Effect of green-Synthesised Fe_3O_4 SPIONs at pH 7 on Eosin Y Degradation

The Fe_3O_4 surface is close to its point of zero charge (pH_{pzc}) at neutral pH (7.0), which lessens

Table 11. Photodegradation of Eosin Y using S/Fe_3O_4 nanohybrid at pH 8. Solar irradiation: 12:00–3:00 pm, 49–52°C, continuous magnetic stirring.

Time (min)	A_o	A_t	%R	A_o/A_t	$\ln(A_o/A_t)$
0	1.642	0	0	0	0
30	1.642	0.260	84.17	6.32	1.84
60	1.642	0.153	90.68	10.73	2.37
90	1.642	0.076	95.37	21.89	3.09
120	1.642	0.034	97.93	48.29	3.88
150	1.642	0.021	98.72	78.19	4.36
180	1.642	0.013	99.21	126.31	4.84

Table 12. Indicates the corrected kinetic and performance parameters of Eosin Y photodegradation at pH 8. All k_{app} and R^2 values are similar to the linear regression fits in Fig. S3 (a, b, c).

Catalyst	A_o	%R (30 min)	%R (180 min)	k_{app} (min^{-1})	R^2	$\ln(A_o/A_t)$ at 180 min
Fe_3O_4 (Green)	1.595	82.32%	99.18%	0.02463	0.9052	4.81
Ag/Fe_3O_4	1.051	88.58%	97.91%	0.01750	0.8115	3.87
S/Fe_3O_4	1.642	84.17%	99.21%	0.02508	0.9491	4.84

the electrostatic interaction between dye and catalyst and inhibits the homogeneous Fenton cycle. Even with these considerations, all three systems achieved high removal efficiencies (98.47–99.10%) at 180 min [50], which suggests that $\bullet O_2^-$ and surface-bound •OH-mediated heterogeneous photocatalytic pathways are still active under solar irradiation at elevated temperatures (49–52°C). The kinetic parameters for all the systems at pH 7 are listed in Table 8.

Effect of Ag/Fe_3O_4 Nanohybrid at pH 7 on Eosin Y Degradation

The Ag/Fe_3O_4 nanohybrid recorded the highest overall performance at pH 7: 94.38% removal within 30 min and 99.10% at 180 min (k_{app} = 0.01977 min^{-1}; Table 6). The pH-independent LSPR mechanism of Ag NPs is a process that keeps pumping hot electrons into the conduction band of Fe_3O_4, no matter what the pH of the bulk solution is. The Schottky barrier precludes back-transferring, which assures efficient charge separation during the irradiation period. The photoactivation effect of LSPR increases the activity of Ag/Fe_3O_4 SPIONs at neutral pH as compared to bare SPIONs [51].

Effect of S/Fe_3O_4 Nanohybrid at pH 7 on Eosin dye

S/Fe_3O_4 showed the best linear kinetic curve at pH 7 with R^2 = 0.8660 and the removal efficiency of 98.86%. The high and stable k_{app} = 0.02045 min^{-1} is indicative of the stable bandgap engineered photocatalysis, where the oxygen vacancies created by sulphur do not deactivate the catalyst and continue to generate •OH and $\bullet O_2^-$ throughout the irradiation window [52].

Pseudo-First-Order Kinetic Analysis and Comparative Performance

Fig. S2 shows the pseudo-first-order kinetic plots for all catalytic systems. The linear behavior of $Ln(A_o/A_t)$ with irradiation time for all the datasets validates the validity of the L–H pseudo-first-order model during the solar irradiation period of 180 min, which is consistent with the previous works of Fe_3O_4-based photocatalysts [53].

At neutral pH, the LSPR-driven hot-electron injection has the maximum kinetic efficiency (k_{app} = 0.01977min^{-1}) and final $Ln(A_o/A_t)$ = 4.71. No reduction was observed after irradiation of the S/Fe_3O_4 sample, which exhibited the most linear (R^2 = 0.8660) catalytic activity. The study reports

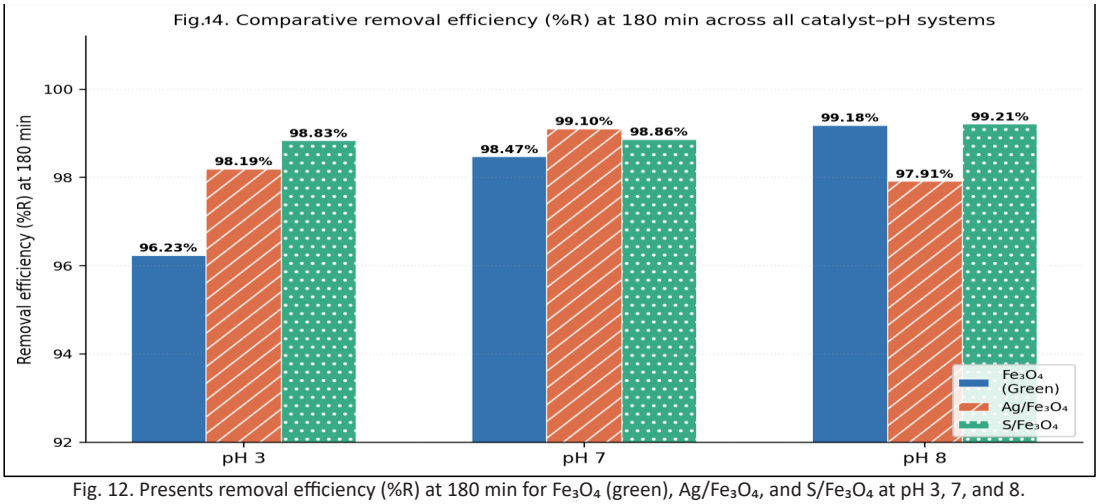

Fig. 12. Presents removal efficiency (%R) at 180 min for Fe_3O_4 (green), Ag/Fe_3O_4, and S/Fe_3O_4 at pH 3, 7, and 8.

Table 13. Summary of %R removal efficiencies at 180 min for all three nanocatalysts at pH 3, 7 and 8; incremental change (Δ) from pH 3 to pH 8; and the optimal pH condition for each nanocatalyst system.

Catalyst	pH 3 (%R)	pH 7 (%R)	pH 8 (%R)	Δ (pH3→pH8)	Best pH
Fe_3O_4 Green	96.23%	98.47%	99.18%	+2.95%	pH 8
Ag/Fe_3O_4	98.19%	99.10%	97.91%	−0.28%	pH 7
S/Fe_3O_4	98.83%	98.86%	99.21%	+0.38%	pH 8

that the green synthesis of surface modification of Fe_3O_4 can overcome the limitations of neutral pH photocatalytic reactions and perform better than the solar dye-removal system [54,55].

Significance of Mildly Alkaline (pH 8) Conditions
Effect of green-Synthesised Fe_3O_4 SPIONs at pH 8 on Eosin Y

The data for the Fe_3O_4 SPIONs are tabulated for A_o = 1.595 at pH 8 in Table 9. The system achieves 99.18% removal at 180 min, its highest value across all three pH conditions studied (pH 3: 96.23%; pH 7: 98.47%; pH 8: 99.18%), with k_{app} = 0.02463 min^{-1} (R^2 = 0.9052) [56].

Mildly alkaline (pH 8) conditions lead to the Fe_3O_4 surface becoming negatively charged due to the presence of a large number of hydroxyl groups (Fe–OH and Fe–O^-). These groups, on the surface, are oxidized by solar photons to produce ferryl radicals (Fe–O•), and the conduction band reduces O_2 to $•O_2^-$. These conditions are especially desirable for Fe_3O_4 and S/Fe_3O_4, which have the highest removal efficiency at pH 8 (Table 10)·[57].

Effect of Ag/Fe_3O_4 Nanohybrid at pH 8 on Eosin Y dye

The Ag/Fe_3O_4 nanohybrid (Table 10, A_o = 1.051) achieved 97.91% removal at 180 min with k_{app} = 0.01750 min^{-1} (R^2 = 0.8115) — the lowest k_{app} and R^2 among the pH 8 systems. There are, however, two context points to consider [58].

The highest k_{app} value was obtained for Green Fe_3O_4 SPIONs at pH 8 (k_{app} = 0.02463 min^{-1}, R^2 = 0.9052), which was the highest value obtained among the three pH values. The Ag/Fe_3O_4 nanohybrid (Table 8, A_o = 1.051) exhibited a relatively low kapp = 0.01750 min^{-1} at pH 8, which is believed to be due to partial passivation of the hydroxyl sites on the Fe_3O_4 by Ag NPs, thereby reducing the beneficial alkaline effect on the generation of $•O_2^-$.[59].

Effect of S/Fe_3O_4 Nanohybrid at pH 8 on Eosin Y dye

Table 11 indicates that the highest k_{app} value (0.02508 min^{-1}), R^2 value (0.9491), and removal efficiency (99.21%) were obtained at pH 8 for S/Fe_3O_4 with an A_o value of 1.642, confirming that this system is the best under alkaline conditions [60].

The reaction may be pH-dependent, with "acid" activation dominating at pH 3, "band-gap narrowing" effects at pH 7 and "alkaline" activation at pH 8. Concurrently, SO_4^{2-} and OH are generated, which in turn results in a dual-radical mechanism that isn't achievable at lower pH. The trend in the k_{app} pH 3 (0.01896) < pH 7 (0.02045) < pH 8 (0.02508 min^{-1}) supports this interpretation. The kinetics are broken down into three steps: medium initiation (0-30 min), fast degradation (30-120 min), and the step of refinement (120-180 min) [61].

Pseudo-First-Order Kinetic Analysis and Comparative Performance/ pH 8

pseudo-first-order kinetic plots of all systems at pH 8. Table 12 reports the values of k_{app} and R^2, which are corrected values obtained directly from these regression lines. All of the values are self-consistent; that is, the slope of each regression line in Fig. S3a, b, c is the same as the corresponding k_{app} value in Table 12 [62,63].

Comparative Removal Efficiency

The photocatalytic removal efficiency (%R) after 180 min is compared for the three noncatalytic systems at pH 3, 7 and 8 in a grouped bar chart, as shown in Fig. 12. The numbers in Table 13 are the values for each system, and the numbers in the column labelled "incremental change" (Δ) show how much these values change from pH 3 to pH 8.

CONCLUSION

The solar-driven photodegradation rate of Eosin Y using green-synthesised nanohybrid composites of Ag/Fe_3O_4 and S/Fe_3O_4 is outstanding over a broad range of pH (3–8) and reaches 96.23–99.21% in 180 min under optimal solar irradiation (49–52°C) without any pH adjustment. Ag/Fe_3O_4 shows the highest rate constant (k_{app} = 0.02139 min^{-1}) at pH 3 due to LSPR-driven charge separation; S/Fe_3O_4 achieves its overall maximum performance at pH 8, with k_{app} = 0.02508 min^{-1} and removal = 99.21% via base-activated dual $SO_4•^-$/•OH radical generation. The results strongly validate the ability of surface modification of green-synthesised Fe_3O_4 to address the mechanistic constraints of each pH domain and suggest that these nanocatalysts are viable, economically competitive, recyclable, and sustainable candidates for actual solar-driven wastewater treatment applications.

ACKNOWLEDGEMENT

The authors would like to thank the Department

of Chemistry in the College of Education for pure sciences, University of Anbar, for providing the required laboratory, facilities, and equipment for conducting this research.

CONFLICT OF INTEREST

The authors declare that there is no conflict of interests regarding the publication of this manuscript.

REFERENCES

1. Abdullateef Abdullahi I, Muhammad Abdullahi I, Ali Gambo Y. Implications of industrial effluents on surface water and ground water. World Journal of Advanced Research and Reviews. 2021;09(03):330-336.
2. Fahad OA. Structural, morphological and antibacterial for cadmium oxide nanoparticles prepared via pulsed laser ablation. Journal of Optics. 2024;55(1):905-912.
3. Ardila-Leal LD, Poutou-Piñales RA, Pedroza-Rodríguez AM, Quevedo-Hidalgo BE. A Brief History of Colour, the Environmental Impact of Synthetic Dyes and Removal by Using Laccases. Molecules. 2021;26(13):3813.
4. Gao T, Qin D, Zuo S, Peng Y, Xu J, Yu B, et al. Decolorization and Detoxification of Triphenylmethane Dyes by isolated endophytic fungus, Bjerkandera adusta SWUSI4 under non-nutritive conditions. Research Square Platform LLC; 2020. http://dx.doi.org/10.21203/rs.3.rs-33850/v1
5. Special occupational hazard review for benzidine-based dyes. U.S. Department of Health, Education, and Welfare, Public Health Service, Centers for Disease Control, National Institute for Occupational Safety and Health; 1980 1980/01/01.
6. Jayeoye TJ. Bionanomaterials-based water remediation techniques. Current Advancements in Nanomaterials for Wastewater Remediation: Elsevier; 2026. p. 113-140. http://dx.doi.org/10.1016/b978-0-443-16112-4.00014-1
7. Berradi M, Hsissou R, Khudhair M, Assouag M, Cherkaoui O, El Bachiri A, et al. Textile finishing dyes and their impact on aquatic environs. Heliyon. 2019;5(11):e02711.
8. Dutta S, Adhikary S, Bhattacharya S, Roy D, Chatterjee S, Chakraborty A, et al. Contamination of textile dyes in aquatic environment: Adverse impacts on aquatic ecosystem and human health, and its management using bioremediation. J Environ Manage. 2024;353:120103.
9. Kumar M, Mishra A, Patel SK, Kushwaha J, Singh S, Mishra V, et al. Environmental Impacts and Strategies for Bioremediation of Dye-Containing Wastewater. Bioengineering. 2025;12(10):1043.
10. Mohammed AS, Fahad OA. Sensitivity enhancement for NO2 gas sensor based on Alq3:TiO_2. AIP Conference Proceedings: AIP Publishing; 2021. p. 040008.
11. Tripathi M, Singh S, Pathak S, Kasaudhan J, Mishra A, Bala S, et al. Recent Strategies for the Remediation of Textile Dyes from Wastewater: A Systematic Review. Toxics. 2023;11(11):940.
12. Hamid NM, Abed HA, Fahad OA. Evaluation of Antibacterial Effects of Silver Nanoparticles Synthesized via Pulsed Laser Ablation at Different Laser Energies. Lasers in Manufacturing and Materials Processing. 2025;12(3):488-497.
13. de Lima CAP, Araujo BA, da Silva KS, Silva CB, de Lima GGC, Vieira FF, et al. Advanced oxidative process by heterogeneous photocatalysis for chemical laboratories effluents treatment. Desalination and Water Treatment. 2020;174:248-257.
14. Jamshidiyan M, Shirani AS, Alahyarizadeh G. Solvothermal synthesis and characterization of magnetic Fe_3O_4 nanoparticle by different sodium salt sources. Materials Science-Poland. 2017;35(1):50-57.
15. Popescu RC, Andronescu E, Vasile BS. Recent Advances in Magnetite Nanoparticle Functionalization for Nanomedicine. Nanomaterials. 2019;9(12):1791.
16. Mahmood A, Ramay SM, Al-Zaghayer YS, AlHazaa A-AN, Al Masary WA, Atiq S. Synthesis and investigation of photocatalytic properties of Au/ Fe_3O_4 nanocomposite materials for degradation of methylene blue. Desalination and Water Treatment. 2016;57(42):20069-20075.
17. Li J, Yang F, Zhou Q, Wu L, Li W, Ren R, et al. Visible-light photocatalytic performance, recovery and degradation mechanism of ternary magnetic Fe_3O_4/BiOBr/BiOI composite. RSC Advances. 2019;9(41):23545-23553.
18. Chakhtouna H, Benzeid H, Zari N, Qaiss Aek, Bouhfid R. Recent progress on Ag/TiO_2 photocatalysts: photocatalytic and bactericidal behaviors. Environmental Science and Pollution Research. 2021;28(33):44638-44666.
19. Guo M, Gao J, Lyu H, Xie Z. Synergistic enhancement of photocatalytic degradation of dyes by structural defects and silver nanoparticles. Dyes and Pigments. 2023;220:111689.
20. Sharif HMA, Mahmood A, Cheng H-Y, Djellabi R, Ali J, Jiang W-L, et al. Fe_3O_4 Nanoparticles Coated with EDTA and Ag Nanoparticles for the Catalytic Reduction of Organic Dyes from Wastewater. ACS Applied Nano Materials. 2019;2(8):5310-5319.
21. Stolbov S, Zuluaga S. Sulfur doping effects on the electronic and geometric structures of graphitic carbon nitride photocatalyst: insights from first principles. J Phys: Condens Matter. 2013;25(8):085507.
22. Patra AR, Pattnaik A, Ghosh P. The latest breakthroughs in green and hybrid nanoparticle synthesis for multifaceted environmental applications. Journal of the Taiwan Institute of Chemical Engineers. 2025:106157.
23. Thatyana M, Dube NP, Kemboi D, Manicum A-LE, Mokgalaka-Fleischmann NS, Tembu JV. Advances in Phytonanotechnology: A Plant-Mediated Green Synthesis of Metal Nanoparticles Using Phyllanthus Plant Extracts and Their Antimicrobial and Anticancer Applications. Nanomaterials. 2023;13(19):2616.
24. Pattoo TA. Flora to Nano: Sustainable Synthesis of Nanoparticles via Plant-Mediated Green Chemistry. Plant Science Archives. 2023;8(1):12-17.
25. Synthesis and Characterization of Fe_3O_4-NPs from Leaves C. Spinosa Extracts and their Anti-Microbial Activity. Nanotechnology Perceptions. 2024;20(3).
26. Okaiyeto K, Ojemaye MO, Hoppe H, Mabinya LV, Okoh AI. Phytofabrication of Silver/Silver Chloride Nanoparticles Using Aqueous Leaf Extract of Oedera genistifolia: Characterization and Antibacterial Potential. Molecules. 2019;24(23):4382.
27. Oluwole AO, Yusuf TL, Tichapondwa SM, Daramola MO, Iwarere SA. Fabrication of $BiVO_4$/Ag_2CrO_4 heterojunction composites modified with graphene oxide for enhanced photoelectrochemical and photocatalytic performance. RSC Advances. 2024;14(51):38044-38058.
28. Mustafa A, Ali U, M, Iqbal A, Qayyum M, Haq IU, et al. Synthesis and Characterization of Fe_3O_4 Nanoparticles by Sol-Gel Method Using Water as a Solvent. Advances in Nanoparticles. 2025;14(01):1-11.
29. Garai C. Green synthesis, characterization and applications of metal nanoparticles. Prayogik Rasayan. 2018;2(3).
30. Bassim S, Mageed AK, AbdulRazak AA. Green Synthesis of Fe_3O_4 Nanoparticles and its Applications in Wastewater Treatment. Research Square Platform LLC; 2022. http://dx.doi.org/10.21203/rs.3.rs-2217120/v1
31. Win TT, Khan S, Bo B, Zada S, Fu P. Green synthesis and characterization of Fe_3O_4 nanoparticles using Chlorella-K01 extract for potential enhancement of plant growth stimulating and antifungal activity. Sci Rep. 2021;11(1).
32. Yoga Darmawan M, Imani Istiqomah N, Adrianto N, Marsel Tumbelaka R, Dwi Nugraheni A, Suharyadi E. Green synthesis

of Fe_3O_4/Ag composite nanoparticles using Moringa oleifera: Exploring microstructure, optical, and magnetic properties for magnetic hyperthermia applications. Results in Chemistry. 2023;6:100999.
33. Eldeeb BA, El-Raheem WMA, Elbeltagi S. Green synthesis of biocompatible Fe_3O_4 magnetic nanoparticles using Citrus Sinensis peels extract for their biological activities and magnetic-hyperthermia applications. Sci Rep. 2023;13(1).
34. Wardani RK, Dahlan K, Wahyudi ST, Sukaryo SG. Synthesis and characterization of nanoparticle magnetite for biomedical application. AIP Conference Proceedings: AIP Publishing; 2019. p. 020137.
35. Ghazanfari MR, Kashefi M, Shams SF, Jaafari MR. Perspective of Fe_3O_4 Nanoparticles Role in Biomedical Applications. Biochem Res Int. 2016;2016:1-32.
36. Jalal AF, Fakhre NA. Preparation and Characterization of Green Fe_3O_4 Nanoparticle Using the Aqueous Plant Extract of Gundelia tournefortii L. Aro-The Scientific Journal Of Koya University. 2021;9(2):58-63.
37. Ajayi RF, Tshoko S, Franke C, Ngema N, Thipe V, Mulaudzi T. Malus domestica and & Solanum lycopersicum Mixtures for the Synthesis of Graphene Silver and Zinc Oxide Nanocomposites. Journal of Surface Engineered Materials and Advanced Technology. 2022;12(04):61-81.
38. Botto IL, Tuti S, Gonzalez MJ, Gazzoli D. Correlation between Iron Reducibility in Natural and Iron-Modified Clays and Its Adsorptive Capability for Arsenic Removal. Advances in Materials Physics and Chemistry. 2016;06(05):129-139.
39. Poh Yan L, Gopinath SCB, Subramaniam S, Chen Y, Velusamy P, Chinni SV, et al. Greener synthesis of nanostructured iron oxide for medical and sustainable agro-environmental benefits. Frontiers in Chemistry. 2022;10.
40. Gutierrez FV, De Falco A, Yokoyama E, Mendoza LAF, Luz-Lima C, Perez G, et al. Magnetic Characterization by Scanning Microscopy of Functionalized Iron Oxide Nanoparticles. Nanomaterials. 2021;11(9):2197.
41. Carmona ER, Sukeri A, Nelson R, Rojo C, Vizcarra A, Villacorta A, et al. Sustainable Green Synthesis of Fe_3O_4 Nanocatalysts for Efficient Oxygen Evolution Reaction. Nanomaterials. 2025;15(17):1317.
42. Yew YP, Shameli K, Miyake M, Kuwano N, Bt Ahmad Khairudin NB, Bt Mohamad SE, et al. Green Synthesis of Magnetite (Fe_3O_4) Nanoparticles Using Seaweed (Kappaphycus alvarezii) Extract. Nanoscale Research Letters. 2016;11(1).
43. Nurdini N, Ilmi MM, Maryanti E, Setiawan P, Kadja GTM, Ismunandar. Thermally-induced color transformation of hematite: insight into the prehistoric natural pigment preparation. Heliyon. 2022;8(8):e10377.
44. Khatun R, Mamun MSA, Islam S, Khatun N, Hakim M, Hossain MS, et al. Phytochemical-Assisted Synthesis of Fe_3O_4 Nanoparticles and Evaluation of Their Catalytic Activity. Micromachines. 2022;13(12):2077.
45. Eslamdoust M, Samari F, Yousefinejad S. One-pot green synthesis of Fe_3O_4@ZnO core–shell nanocomposites with multifunctional properties. Sci Rep. 2025;15(1).
46. Balakrishna M, Mamidi G, Botsa SM, Kumar GP. Enhanced Photocatalytic Degradation of Eosin Yellow Dye using Fe_3O_4 Nanoparticles from S. prostrata Leaf Extract and their Cytotoxicity against MCF-7 Cell Line. Asian J Chem. 2025;37(12):3055-3064.
47. Senthilmurugan B, Okla MK, Abdel-Maksoud MA, Al-Amri SS, Alaraidh IA, Alatar AA, et al. Interface engineered Ag-r-GO-$CuFe_2O_4$-Fe_3O_4heterojunction an efficient photocatalyst for water treatment and toxicity study in Trifolium plants. Journal of Industrial and Engineering Chemistry. 2024;135:344-355.
48. Wu R, Wang Y, Wang J, Tian G, Li Y, Liu C. Facile preparation of Fe_3O_4/HAP/Ag nanomaterial and photocatalytic degradation of four types of dyes with mechanism. RSC Advances. 2025;15(33):27128-27138.
49. Tang X, Li Z, Liu K, Luo X, He D, Ao M, et al. Sulfidation modified Fe_3O_4nanoparticles as an efficient Fenton-like catalyst for azo dyes degradation at wide pH range. Powder Technol. 2020;376:42-51.
50. Mallah S, El Mchaouri M, El Meziani S, Agnaou H, El Haddaj H, Boumya W, et al. Green Photocatalysis: A Comprehensive Review of Plant-Based Materials for Sustainable Water Purification. Reactions. 2025;6(4):55.
51. Pant B, Park M, Lee JH, Kim H-Y, Park S-J. Novel magnetically separable silver-iron oxide nanoparticles decorated graphitic carbon nitride nano-sheets: A multifunctional photocatalyst via one-step hydrothermal process. Journal of Colloid and Interface Science. 2017;496:343-352.
52. Ramos-Justicia JF, Urbieta A, Fernández P. Refined Langmuir–Hinshelwood Kinetics for Heterogeneous Photocatalytic Systems: Analytical Closed-Form Solution, Enhanced Approximations and Experimental Validation. Physchem. 2026;6(1):5.
53. Mahich S, Shekhawat KS, Gupta S, Kumar A, Swami SK, Mathur J, et al. Synthesis and Characterization of Eco-Friendly Fe_3O_4/g-C_3N_4/rGO Nanocomposites for Photodegradation of Methylene Blue Dye. Advances in Nanoparticles. 2025;14(04):121-141.
54. Khan S, Noor T, Iqbal N, Yaqoob L. Photocatalytic Dye Degradation from Textile Wastewater: A Review. ACS Omega. 2024;9(20):21751-21767.
55. Chakravorty A, Roy S. A review of photocatalysis, basic principles, processes, and materials. Sustainable Chemistry for the Environment. 2024;8:100155.
56. Bazrafshan E, Mohammadi L, Zarei AA, Mosafer J, Zafar MN, Dargahi A. Optimization of the photocatalytic degradation of phenol using superparamagnetic iron oxide (Fe_3O_4) nanoparticles in aqueous solutions. RSC Advances. 2023;13(36):25408-25424.
57. Xu T, Zhu R, Zhu G, Zhu J, Liang X, Zhu Y, et al. Mechanisms for the enhanced photo-Fenton activity of ferrihydrite modified with BiVO4 at neutral pH. Applied Catalysis B: Environmental. 2017;212:50-58.
58. Jiang P, Wang K, Liu W, Song Y, Zheng R, Chen L, et al. Hot Electrons Induced by Localized Surface Plasmon Resonance in Ag/g-C_3N_4 Schottky Junction for Photothermal Catalytic CO2 Reduction. Polymers. 2024;16(16):2317.
59. Sen S, Das C, Ghosh NN, Baildya N, Bhattacharya S, Khan MA, et al. Is degradation of dyes even possible without using photocatalysts? – a detailed comparative study. RSC Advances. 2022;12(53):34335-34345.
60. Nadeem S, Bukhari M, Javed M, Iqbal S, Ahmad MN, Alrbyawi H, et al. Cation Incorporation and Synergistic Effects on the Characteristics of Sulfur-Doped Manganese Ferrites S@Mn(Fe_2O_4) Nanoparticles for Boosted Sunlight-Driven Photocatalysis. Molecules. 2022;27(22):7677.
61. Gao W, Li B, Shao Y, Li G, Wang C, Li N, et al. Free radical switching behavior between initial neutral and buffer neutral condition during Fenton-like degradation over pyrite/hematite mineral. Environ Res. 2025;286:122759.
62. Mohamed MS, Hozayen WG, Alharbi RM, Ibraheem IBM. Adsorptive recovery of arsenic (III) ions from aqueous solutions using dried Chlamydomonas sp. Heliyon. 2022;8(12):e12398.
63. Ibikunle PD, Elemile OO, Ejigboye PO, Bala DO, Olawolu AP, Adebayo AA, et al. Removal of hexavalent chromium from contaminated synthetic groundwater via functionalized carbon nanomaterials modified with zinc and potassium. Sci Rep. 2025;15(1).